JOURNAL OF COMPUTATIONAL PHYSICS 101, 231–251 (1992)

A Hybrid Finite-Boundary Element Method for Inviscid Flows with Free Surface

N. A. PELEKASIS,* J. A. TSAMOPOULOS,*,[1] AND G. D. MANOLIS†

*Departments of *Chemical and †Civil Engineering, State University of New York at Buffalo, Buffalo, New York 14260*

Received December 9, 1990; revised November 8, 1991

Different formulations of free-surface inviscid flows lead to Fredholm integral equations of the first or second kind. In the present study, these formulations are compared in terms of efficiency and accuracy when different time and space discretization schemes are employed in studying inviscid oscillations of a liquid drop. A hybrid scheme results from combining a boundary integral equation approach for the Laplacian with a Galerkin/finite-element technique for the kinematic and dynamic boundary conditions. It is found that the fourth-order Runge–Kutta method is the most efficient among various schemes tested for integration in time and that cubic splines should be preferred as basis functions over conventional Lagrangian basis functions. Furthermore, the formulation based on the integral equation of the second kind is found to be more prone to short-wave instabilities. However, if numerical filtering is applied in conjunction with it, then the time-step used can be twice as large as that required by the unfiltered integral equation of the first kind. Results compare well with analytic solutions in the form of asymptotic expansions.

1. INTRODUCTION

Quite often, potential flow problems are treated numerically using integral equations. Existence of solutions to such equations was first proved by Fredholm [1]. Fredholm integral equations of the first or second kind follow from the representation of harmonic functions by either single-layer or double-layer potentials, respectively. Kellogg [2], in his classical treatise on potential theory, used this integral formulation extensively. Another approach, which received no mention in Kellogg, is through Green's third identity. It represents harmonic functions as the superposition of both single- and double-layer potentials. An extensive review of the theory and a numerical implementation of the latter approach can be found in Jaswon and Symm [3].

Potential flow problems involving free surface motion are also amenable to an integral formulation. The complexity of boundary conditions on the free surface, however, made any serious application impractical for a long time. The advent of computers of reasonable speed in the late 1960s allowed for further exploitation of the integral equation approach in the area of fluid mechanics and especially for free surface flows. In integral formulations generally, the potential and all other quantities describing the flow in the bulk can be given in terms of their respective boundary values. Thus, discretization of the entire domain is avoided and the dimensionality of the problem is reduced by one. This important property along with the ability of integral formulations to satisfy certain boundary conditions, through use of appropriate single- and double-layer potentials, constitute a great advantage over conventional numerical techniques such as finite differences and finite elements.

There are various ways of implementing an integral equation formulation. For instance, Longuet-Higgins and Cokelet [4], in their study of steady and breaking surface waves, used a Lagrangian representation of the surface and a fourth-order explicit Adams–Bashforth scheme in order to advance the location of the free boundary. The normal velocity of the surface was given as the solution to an integral equation of the first kind. This method, however, produced a short-wave instability. Smoothing by introduction of artificial viscosity permitted integration in time. Grilli *et al.* [5] extended the method developed by Dold and Peregrine [6] to account for three-dimensional nonperiodic water waves. In particular, they used Green's formula as opposed to Cauchy's theorem which is limited to two-dimensional waves.

As far as time integrations were concerned, they proceeded like Dold and Peregrine in the following way: First, the boundary integral equation was used to calculate the Eulerian time-derivatives up to a certain order. Next, the Lagrangian time-derivatives were calculated using boundary conditions and the potential and boundary location were updated. Finally, an integral equation of the first kind was solved for the normal velocity. Smoothing was not required for integrating up to the reported time. In their study of forced oscillations of solid bodies on water surfaces, Dommermuth and Yue [7] employed Green's theorem to solve for the normal velocity in conjunction with the fourth-order Runge–Kutta method. In order to avoid concentra-

[1] To whom correspondence should be addressed.

0021-9991/92 $5.00

tion of Lagrangian markers in regions of high curvature which accelerates growth of instabilities, remeshing was performed after every time-step. This is a form of smoothing and a rather expensive operation. Blake *et al.* [8, 9] did not have to resort to any form of smoothing, however, in their study on the motion of transient cavities near rigid boundaries and free surfaces. They also used Green's theorem along with linear Lagrangian basis functions and the explicit Euler time integration scheme.

For two-dimensional flows, differentiation of the integral equation for the complex potential results in an integral representation for the complex velocity in terms of a vortex-sheet. This leads to an integral equation of the second kind for the vortex-sheet strength as well as the boundary location and the potential distribution. The point vortex method has been widely used, since Rosenhead's [10] and Birkhoff's [11] studies of the motion of a vortex-sheet in a constant density fluid in the context of numerical simulations of layered flows. Such flows are known to be subject to Kelvin–Helmholtz (K–H) or Rayleigh–Taylor (R–T) instabilities. In numerical studies of R–T instabilities, Pullin [12] and others have found chaotic vortex behavior in regions where smooth rolling of the vortex-sheet should have been expected. Chaotic behavior has also been observed in conjunction with K–H instability by Pullin [12] and Krasny [13]. In all these studies, chaotic motion was associated with the growth of short waves and smoothing had to be applied. Moore [14] argued that the above observations are due to R–T and K–H instabilities in the discrete forms of the equations, thus supporting an earlier conjecture by Birkhoff [11].

Baker *et al.* [15, 16] used a generalized point vortex method for studying either R–T instabilities or plunging breaker waves. They also observed short-wave growth, but suppressed it by decreasing the time-step and limiting the length of integration in time. Using a similar method, Moore [17] observed a rapid growth of high modes, even though for the flow examined no unstable eigenvalues existed in the linear limit. He attributed it to a resonant interaction between the higher and lower modes due to numerical inaccuracy in the dispersion relation. Later Baker *et al.* [18] extended their method to account for axisymmetric and three-dimensional flows. They observed that a representation of the free surface by a distribution of dipoles is better for short-wave instabilities as opposed to a distribution of point vortices. They also argued that their method should be preferred because it leads to an integral equation of the second kind which can be solved iteratively with increased savings in computer-time. This is possible because the system matrix resulting from discretization of an integral equation of the second kind is diagonally dominant. The same argument was put forth by Karrila and Kim [19] for problems in creeping flow.

In studying free-surface flows it is often most important to integrate for very long time in order to capture the nonlinear effects as accurately as possible. It has been found that particularly demanding test-problems are those associated with theoretical predictions of phenomena observed in oscillating simple and compound drops [20, 21]. Experimental results have been obtained by several investigators, e.g., [22–25], who suspended liquid drops in a neutrally buoyant liquid or in the reduced gravity environment in space. Thus, the linear oscillation frequencies predicted by [26, 27] have been confirmed and they have been observed to decrease with the square of the amplitude of the motion. This last effect was explained by Tsamopoulos and Brown [27, 28] in their asymptotic analysis that is valid for weakly nonlinear oscillations. For the same problems, numerical simulations have been conducted [29, 30] using the marker and cell finite-difference technique, which is very tedious and expensive. In addition, Benner [31] used finite elements for large-amplitude drop oscillations. Finally, Lundgren and Mansour [32] used the approach suggested by Baker *et al.* [16, 18] that has all the advantages of a boundary integral formulation, but still requires filtering to suppress the rapid growth of high modes.

In view of the variety of integral representations, the space and time discretization schemes available and the numerical difficulties mentioned above, choosing the best combination for a given problem becomes a difficult task. For this reason we focus on comparisons, in terms of accuracy and efficiency between integral equation formulations of the first and second kind as well as of various explicit and implicit time integrators. For spatial discretization, boundary elements (BE) are used for the integral equation in conjunction with finite elements (FE) for the boundary conditions. This results in a hybrid method that combines the best features of both FE and BE. Furthermore, in an effort to obtain a good representation of the dependent variables so as to suppress possible numerical instabilities, the cubic *B*-splines are compared with quadratic Lagrangian basis functions.

In Section 2, the Eulerian formulation in terms of canonical variables is given. Assuming that the drop surface does not fold over itself, the Eulerian representation is advantageous since it prevents uneven distribution of mesh points, which is known to cause growth of short-wave instabilities [7, 14, 32]. The Laplacian is recast as an integral equation of the first or second kind in Section 3. Different numerical methodologies are discussed in Section 4, while numerical results are presented and discussed in Section 5. Conclusions are drawn in Section 6.

2. EULERIAN FORMULATION IN TERMS OF CANONICAL VARIABLES

The irrotational and incompressible motion of an inviscid liquid drop in a zero-gravity environment is considered. The

drop is surrounded by a tenuous gas. Thus, its dynamics are decoupled from those of the surrounding medium and the inviscid assumption is physically and mathematically justifiable as long as the Reynolds number is large [28]. The drop density is ρ and the interfacial tension is σ. The surface of the drop during motion is described by $\bar{R}F(\theta, t)$, where $\bar{R}$ is the dimensional radius of a sphere with the same volume as the drop, $F(\theta, t)$ is the dimensionless shape-function of the drop, and θ is the meridianal angle in spherical coordinates. Velocity potential, pressure, and time are rendered dimensionless with scales based on the results of linear analysis; $\Phi(r, \theta, t) = \bar{\Phi}/(\sigma\bar{R}/\rho)^{1/2}$, $P(r, \theta, t) = \bar{P}/(2\sigma/\bar{R})$, $t = \bar{t}/(\rho\bar{R}^3/\sigma)^{1/2}$. The dimensionless radial coordinate is scaled with the equilibrium radius of the drop. Since only axisymmetric disturbances are considered, the boundary reduces to a curve, namely, the generating curve of the drop surface. The outward pointing normal vector $\mathbf{n}$ is given with respect to unit vectors in spherical coordinates, $\mathbf{e}_r$, $\mathbf{e}_\theta$, by

$$\mathbf{n} = \frac{(F\mathbf{e}_r - F_\theta \mathbf{e}_\theta)^{1/2}}{F^2 + F_\theta^2} = n_r \mathbf{e}_r + n_\theta \mathbf{e}_\theta, \tag{1}$$

where $F_\theta = \partial F/\partial\theta$.

The governing equations in differential form are given elsewhere [21, 28]. The goal of the present approach, however, is to reformulate the problem in terms of quantities defined on the boundary only. To this end, the value of the potential on the free surface is introduced as a new dependent variable, i.e.,

$$\psi(\theta, t) \equiv \Phi(r = F(\theta, t), \theta, t). \tag{2}$$

The potential, $\psi(\theta, t)$, the drop shape function, $F(\theta, t)$, and the velocity normal to the interface, $\partial\Phi/\partial n$, constitute the only dependent variables of the problem. Zakharov [33] and Miles [34], independently, showed that the potential of the free surface and the free-surface location are the canonical variables of the Hamiltonian formulation for gravity water waves in two dimensions. They also showed that these two quantities are the most appropriate for description of the motion and used their spectral representation in order to study the stability of periodic waves.

The chain rule for differentiation is used in order to evaluate derivatives of $\psi(\theta, t)$ with respect to t or θ. For example,

$$\left.\frac{\partial\psi}{\partial\theta}\right|_t = \left.\frac{\partial\Phi}{\partial\theta}\right|_{t, r, r = F(\theta, t)} + \left.\frac{\partial\Phi}{\partial r}\right|_{\theta, t, r = F(\theta, t)} \left.\frac{\partial F}{\partial\theta}\right|_t, \tag{3}$$

and similarly for $\partial\psi/\partial t|_\theta$. By combining Eqs. (1) and (3) with the gradient operator in spherical coordinates, $\partial\Phi/\partial r|_{\theta, t, r = F(\theta, t)}$ can be expressed in terms of the normal and meridianal derivatives of the potential,

$$\left.\frac{\partial\Phi}{\partial r}\right|_{\theta, t, r = F(\theta, t)} = \left(\frac{\partial\psi}{\partial\theta}\frac{\partial F}{\partial\theta}\right)\Big/(F^2 + F_\theta^2) + \left(\frac{\partial\Phi}{\partial n}F\right)\Big/(F^2 + F_\theta^2)^{1/2}, \quad 0 \leqslant \theta \leqslant \pi. \tag{4}$$

Substitution of Eqs. (3) and (4) in the usual kinematic condition [21] yields

$$\frac{\partial F}{\partial t} = \frac{\partial\Phi}{\partial n}\left(1 + \frac{F_\theta^2}{F^2}\right)^{1/2}, \qquad 0 \leqslant \theta \leqslant \pi. \tag{5}$$

There are other ways to arrive at the above equation; for example, one can combine the kinematic condition with the definition for the free surface and the normal velocity. However, the derivation given here is identical to that needed for the dynamic boundary condition as well.

Next, Bernoulli's equation is evaluated at the free surface and the pressure in the liquid is eliminated after introduction of the normal force balance,

$$2P_0 - 2\mathscr{H} + \frac{\partial\Phi}{\partial t} + \frac{1}{2}|\nabla\Phi|^2 = 0, \qquad r = F(\theta, t), \quad 0 \leqslant \theta \leqslant \pi, \tag{6}$$

where P_0 is the constant gaseous pressure and $\mathscr{H}$ is the mean curvature of the surface given by

$$-2\mathscr{H} = \left[-\frac{F_{\theta\theta}}{F} - \cot\theta\frac{F_\theta}{F}\left(1 + \frac{F_\theta^2}{F^2}\right) + 2 + 3\frac{F_\theta^2}{F^2}\right] \times \left[F\left(1 + \frac{F_\theta^2}{F^2}\right)\right]^{-1}. \tag{7}$$

Using Eqs. (3) and (4) in Eq. (6), a new form of the dynamic boundary condition is obtained that is entirely dependent on surface quantities,

$$2\mathscr{H} = \frac{\partial\psi}{\partial t} + 2P_0 - \frac{1}{2}\left(\frac{\partial\Phi}{\partial n}\right)^2 + \frac{1}{2}\left(\frac{\partial\psi}{\partial\theta}\right)^2\frac{1}{F^2 + F_\theta^2} - \frac{\partial\Phi}{\partial n}\frac{\partial\psi}{\partial\theta}\frac{F_\theta}{F(F^2 + F_\theta^2)^{1/2}}. \tag{8}$$

The normal derivative of the potential is yet to be related to the potential at the free surface. This is done by using

Laplace's equation and is discussed in the next section. Schematically one can write this relationship as

$$L\left(\psi, \frac{\partial \Phi}{\partial n}\right) = 0. \tag{9}$$

It should be noted that there is an important advantage in the formulation presented above. Since the radial coordinate has dropped out of the equations, partial derivatives with respect to t or θ are now taken with constant θ or t, respectively. In the original differential formulation, r had to be held constant as well, which resulted in some ambiguity, when it came to numerical differentiation with respect to θ or t. Furthermore, the current formulation makes apparent the one-dimensional character of the problem and the numerical implementation is simplified. In summary, the three dependent variables, ψ, F, and $\partial\Phi/\partial n$, are calculated by Eqs. (8), (5), and (9), respectively.

When the drop is perturbed from a spherical configuration no initial velocity is imparted to it,

$$\frac{\partial F}{\partial t}(\theta, t=0) = 0, \tag{10}$$

so that the motion is initially irrotational and remains so in the absence of viscosity. The initial perturbation consists of a deformation of the interface that preserves the volume of the drop. In order to compare with results of asymptotic analysis [28], the initial deformation

$$F(\theta, t=0) = 1 + \varepsilon P_n(\theta) + \mathcal{O}(\varepsilon^2) \tag{11}$$

may be assumed, where $P_n(\theta)$ are Legendre Polynomials of order n and ε is a measure of the disturbance.

Irrespective of the initial disturbance certain quantities remain invariant during motion. They are:

(a) The volume of the incompressible drop,

$$V = \frac{2\pi}{3}\int_0^\pi F^3 \sin\theta \, d\theta = \frac{4\pi}{3}. \tag{12}$$

In view of the truncated expansion series used for the initial location of the boundary, the volume of the drop is slightly different from $4\pi/3$ initially and it will remain so forever, owing to the incompressibility of the liquid.

(b) The total mass outflux across the free surface, which must remain zero due to mass conservation,

$$I = \int_S \frac{\partial \Phi}{\partial n} dA = 2\pi \int_0^\pi \frac{\partial \Phi}{\partial n} F(F^2 + F_\theta^2)^{1/2} \sin\theta \, d\theta = 0. \tag{13}$$

This can be shown analytically by using Gauss' theorem on the Laplacian, and

(c) The total energy which is composed of the kinetic, E_k and surface, E_S, energies

$$\begin{aligned} E = E_k + E_S &= \frac{1}{2}\int_V |\nabla\Phi|^2 \, dV + \int_A dA \\ &= \pi \int_0^\pi \Phi \frac{\partial \Phi}{\partial n} F(F^2 + F_\theta^2)^{1/2} \sin\theta \, d\theta \\ &\quad + 2\pi \int_0^\pi F(F^2 + F_\theta^2)^{1/2} \sin\theta \, d\theta = 4\pi. \end{aligned} \tag{14}$$

The total energy must remain equal to the surface energy of an undisturbed spherical drop. These invariants offer excellent checks for the global accuracy of any numerical scheme.

3. INTEGRAL FORMULATIONS

In order to relate the velocity potential on the drop surface with the normal velocity to it, the Laplacian is replaced by an equivalent integral equation. There are two ways of doing this.

3.1. *Direct Application of Green's Theorem*

The three-dimensional singular solution of the Laplacian at the field point $\mathbf{x}'(r', \theta', \phi')$ subject to α point force at the source point $\mathbf{x}(r, \theta, \phi)$ is given by

$$\begin{aligned} \hat{G}(\mathbf{x}, \mathbf{x}') = \frac{1}{4\pi}\frac{1}{|\mathbf{x} - \mathbf{x}'|} = \frac{1}{4\pi}\,[&(r\sin\theta\cos\phi - r'\sin\theta'\cos\phi')^2 \\ &+ (r\sin\theta\sin\phi - r'\sin\theta'\sin\phi')^2 \\ &+ (r\cos\theta - r'\cos\theta')^2]^{-1/2}. \end{aligned} \tag{15}$$

Application of Green's formula gives

$$\begin{aligned} \alpha\Phi(\mathbf{x}', t) + \oint_A \Phi(\mathbf{x}, t)\frac{\partial \hat{G}}{\partial n}(\mathbf{x}, \mathbf{x}')\, dA(\mathbf{x}, t) \\ = \oint_A \frac{\partial \Phi}{\partial n}(\mathbf{x}, t)\, \hat{G}(\mathbf{x}, \mathbf{x}')\, dA(\mathbf{x}, t), \end{aligned} \tag{16}$$

where A is the surface enclosing the drop, and $\partial\hat{G}/\partial n$ is the derivative of $\hat{G}$ with respect to the outward pointing normal. If the field point lies in the interior (exterior) of the drop, the coefficient of the jump term, α, is equal to 1.0 (0.0). If it lies on the surface, then it is given by the solid angle (measured in multiples of 4π) under which the domain occupied by the fluid is seen from that point (e.g., $\alpha = \frac{1}{2}$ for a smooth surface). In this case, the field point may coincide with one of the source points, thus rendering the integrals in Eq. (16) singular. As explained in the next section, the singularity in the $\hat{G}$ kernel is weak and hence integrable, whereas the one

in $\partial\hat{G}/\partial n$ is only integrable in the Cauchy principal value sense.

In order to isolate the singularity in the integrand involving $\partial\hat{G}/\partial n$, the value of the potential at the field point is added and subtracted in Eq. (16) resulting in

$$\oint_A \frac{\partial \Phi}{\partial n}(\mathbf{x}, t)\,\hat{G}(\mathbf{x}, \mathbf{x}')\,dA(\mathbf{x}, t) = \alpha\Phi(\mathbf{x}', t) + \int_A \Phi(\mathbf{x}', t)\frac{\partial \hat{G}}{\partial n}(\mathbf{x}, \mathbf{x}')\,dA(\mathbf{x}, t) + \oint_A [\Phi(\mathbf{x}, t) - \Phi(\mathbf{x}', t)] \times \frac{\partial \hat{G}}{\partial n}(\mathbf{x}, \mathbf{x}')\,dA(\mathbf{x}, t). \quad (17)$$

Now the integrand in the second integral of the LHS of Eq. (17) is weakly singular, because when field and source points coincide, the difference between $\Phi(\mathbf{x}, t)$ and $\Phi(\mathbf{x}', t)$ goes to zero as $|\mathbf{x}-\mathbf{x}'|$. Combining this fact with the $\mathcal{O}(|\mathbf{x}-\mathbf{x}'|^{-2})$ singularity in $\partial\hat{G}/\partial n$ renders the aforementioned integrand integrable. Since $\Phi(\mathbf{x}', t)$ is a constant with respect to integration over all source points on the surface, the first integral in the RHS of Eq. (17) simplifies to a well known principal value integral [3],

$$\Phi(\mathbf{x}', t)\int_A \frac{\partial \hat{G}}{\partial n}(\mathbf{x}, \mathbf{x}')\,dA(\mathbf{x}, t) = -\frac{1}{2}\Phi(\mathbf{x}', t). \quad (18)$$

Thus, Eq. (17) becomes

$$\oint_A [\Phi(\mathbf{x}, t) - \Phi(\mathbf{x}', t)]\frac{\partial \hat{G}}{\partial n}(\mathbf{x}, \mathbf{x}')\,dA(\mathbf{x}, t) = \oint_A \frac{\partial \Phi}{\partial n}(\mathbf{x}, t)\,\hat{G}(\mathbf{x}, \mathbf{x}')\,dA(\mathbf{x}, t). \quad (19)$$

For axisymmetric problems the potential is independent of ϕ, consequently ϕ' can be set to zero for simplicity, and the integration of the kernels with respect to ϕ can be carried out giving

$$\int_0^{\pi} [\psi(\theta, t) - \psi(\theta', t)] \times \frac{\partial G}{\partial n}(F, F', \theta, \theta')\,F(F^2 + F_\theta^2)^{1/2}\sin\theta\,d\theta = \int_0^{\pi} \frac{\partial \Phi}{\partial n}(\theta, t)\,G(F, F', \theta, \theta') \times F(F^2 + F_\theta^2)^{1/2}\sin\theta\,d\theta, \quad (20)$$

where

$$G = \int_0^{2\pi} \hat{G}\,d\phi \quad \text{and} \quad \frac{\partial G}{\partial n} = \int_0^{2\pi} \frac{\partial \hat{G}}{\partial n}\,d\phi. \quad (21)$$

These two kernels can be written in terms of elliptic integrals of the first and second kind as is shown in the next section. When Eq. (20) is used to calculate $\partial\Phi/\partial n$ (Dirichlet's problem), it constitutes a Fredholm integral equation of the first kind. This is a well posed problem [3]. However, as Baker and Shelley [35] point out, it must be solved by direct inversion since matrix splitting that would lead to an iterative scheme is not possible. Direct matrix inversion of fully populated matrices, such as those generated here, is widely performed by standardized routines. The cost for inversion, however, increases as n^3, where n is the number of equations generated by discretization in space. In addition, a marked increase of the condition number of the system matrix has been observed which results in reduction of accuracy. Fortunately, the mesh size required for the present study remained small enough so that this effect did not dominate the solution procedure and results of high quality could still be obtained. It should also be noted that both ψ and $\partial\Phi/\partial n$ appear in Eq. (20) and, if it is solved simultaneously with Eqs. (5) and (8) for calculating ψ, F, and $\partial\Phi/\partial n$, it cannot be classified as a Fredholm equation of either the first or second kind.

3.2. *Indirect Formulation by Using a Dipole Distribution*

An alternative approach for solving the Dirichlet problem is to use an integral equation of the second kind. This was originally proposed by Baker *et al.* [18] and more recently employed by Lundgren and Mansour [32]. At first, the potential is given in terms of a distribution of double layer potentials, μ, as follows:

$$\Phi(\mathbf{x}', t) = \alpha\mu(\mathbf{x}', t) + \oint_A \mu(\mathbf{x}, t)\frac{\partial \hat{G}}{\partial n}(\mathbf{x}, \mathbf{x}')\,dA(\mathbf{x}, t). \quad (22)$$

Alternatively, when the flow is incompressible, the velocity can be derived from a vector potential, $\mathbf{T}$:

$$\mathbf{v} = \nabla \times \mathbf{T}. \quad (23)$$

Therefore, the velocity normal to the drop surface may be given either in terms of the scalar potentials Φ, or the vector potential, $\mathbf{T}$:

$$\mathbf{v}\cdot\mathbf{n} = \frac{\partial \Phi}{\partial n} = (\mathbf{n}\times\nabla)\cdot\mathbf{T}. \quad (24)$$

Even though the motion is irrotational inside the drop, there is a discontinuity in the velocity field generated by the

double layer potential as the interface is crossed. Consequently, the free surface can be viewed as a vortex sheet with circulation density γ which according to [36] is given by

$$\mathbf{T}(\mathbf{x}', t) = \oint_A \gamma(\mathbf{x}, t)\, \hat{G}(\mathbf{x}, \mathbf{x}')\, dA(\mathbf{x}, t). \tag{25}$$

Comparison of the expression for velocity in terms of the double-layer potential with the one resulting from the circulation and after some algebra yields a relationship between γ and μ:

$$\gamma = -\mathbf{n} \times \nabla_S \mu. \tag{26}$$

Substitution of Eq. (26) into Eq. (25) and application of Gauss' theorem gives

$$\mathbf{T}(\mathbf{x}', t) = \oint_A [\mathbf{n}(\mathbf{x}, t) \times \nabla \hat{G}(\mathbf{x}, \mathbf{x}')]\, \mu(\mathbf{x}, t)\, dA(\mathbf{x}, t). \tag{27}$$

As a result of these manipulations, the indirect method proceeds by calculating the double-layer potential distribution from the scalar potential using Eq. (22), the vector potential from the double-layer potential using Eq. (27), and finally the normal velocity at the surface from the vector potential using Eq. (24).

Similarly to the direct method, when the field point is taken onto the smooth surface, the integrals in Eqs. (22) and (27) become

$$\Phi(\mathbf{x}', t) = -\frac{1}{2}\mu(\mathbf{x}', t) + \int_A \mu(\mathbf{x}, t) \frac{\partial \hat{G}}{\partial n}(\mathbf{x}, \mathbf{x}')\, dA(\mathbf{x}, t) \tag{28}$$

and

$$\mathbf{T}(\mathbf{x}', t) = \int_A \mu(\mathbf{x}, t)[\mathbf{n}(\mathbf{x}, t) \times \nabla \hat{G}(\mathbf{x}, \mathbf{x}')]\, dA(\mathbf{x}, t), \tag{29}$$

respectively, where $-\frac{1}{2}$ and 0 are the jump term coefficients corresponding to the singular kernels $\partial \hat{G}/\partial n$ and $\mathbf{n} \times \nabla \hat{G}$. The remaining integrals in Eqs. (28) and (29) are now understood in the Cauchy principal value sense. In order to extract the singular part of the kernels and render these integrands integrable, a procedure similar to that for the direct method is followed. Thus,

$$\Phi(\mathbf{x}', t) = -\mu(\mathbf{x}', t) + \oint_A [\mu(\mathbf{x}, t) - \mu(\mathbf{x}', t)] \times \frac{\partial \hat{G}}{\partial n}(\mathbf{x}, \mathbf{x}')\, dA(\mathbf{x}, t) \tag{30}$$

and

$$\mathbf{T}(\mathbf{x}', t) = \int_A [\mu(\mathbf{x}, t) - \mu(\mathbf{x}', t)] \times [\mathbf{n}(\mathbf{x}, t) \times \nabla \hat{G}(\mathbf{x}, \mathbf{x}')]\, dA(\mathbf{x}, t). \tag{31}$$

The new integrands are weakly singular, since $(\mu - \mu')$ goes to zero as $|\mathbf{x} - \mathbf{x}'|$, whereas the kernels above vary as $|\mathbf{x} - \mathbf{x}'|^{-2}$.

For the case of axisymmetric flows, ϕ' may again be set to zero and the integrations with respect to ϕ are carried out yielding

$$\psi(\theta', t) = -\mu(\theta, t) + \int_0^{\pi} [\mu(\theta, t) - \mu(\theta', t)] \times \frac{\partial G}{\partial n}(F, \theta, F', \theta')\, F(F^2 + F_\theta^2)^{1/2} \sin\theta\, d\theta \tag{32}$$

and

$$\mathbf{T}(\theta', t) = \mathbf{e}_\phi \int_0^{\pi} [\mu(\theta, t) - \mu(\theta', t)] \times \tilde{G}(F, \theta, F', \theta')\, F(F^2 + F_\theta^2)^{1/2} \sin\theta\, d\theta, \tag{33}$$

where $\partial G/\partial n$ is given by Eq. (21) and

$$\mathbf{e}_\phi \tilde{G} = \int_0^{2\pi} \mathbf{n} \times \nabla \tilde{G}\, d\phi. \tag{34}$$

The specific expression for the kernel $\tilde{G}$ is given in the next section. Having obtained the single nonzero component of $\mathbf{T}$, $(T_\phi \mathbf{e}_\phi)$, the normal velocity is calculated by simplifying Eq. (24):

$$\frac{\partial \Phi}{\partial n} = \left[\frac{\partial T_\phi}{\partial \theta} + \frac{T_\phi (F \cos\theta + F_\theta \sin\theta)}{F \sin\theta}\right](F^2 + F_\theta^2)^{-1/2}. \tag{35}$$

Given the potential on the free surface, Eq. (32) is a Fredholm integral equation of the second kind for the dipole distribution μ. Its homogeneous part has no nontrivial solutions [3] and it can be solved using an iterative process without further complications. This is preferable over a direct matrix inversion for large problems. Compared to Green's method, this advantage is attenuated by the extra time required for construction of twice as many system matrices.

4. NUMERICAL SOLUTION

Due to the integral formulation and the introduction of canonical variables, discretization in only one space dimension is required. The absence of any region on the free surface where abrupt changes occur permits the use of an equidistant mesh in θ and constant time steps.

4.1. *Finite-Element Implementation*

The Galerkin/finite-element method is used for transforming the kinematic and dynamic boundary conditions from partial differential equations to initial value equations. To this end, the corresponding unknown variables (F, ψ) are represented as a finite sum of unknown coefficients multiplied by a set of prespecified basis functions that are nonzero only over a few elements of the domain. The weak formulation results upon multiplication of Eqs. (5) and (8) by each basis function in turn and integration over the domain. Integration by parts is also carried out in order to eliminate the second derivative, appearing in the surface curvature term. Four Gauss integration points are used for the evaluation of integrals over each element. This ensures that any numerical error is controlled by the interpolation of unknown functions rather than by numerical integration [37].

Two different basis functions are used, the quadratic Lagrangian polynomials and the cubic *B*-splines. The former functions are nonzero over two elements at most, and guarantee continuity of the dependent variable only [38]. As a result, they are constructed so that the value of the interpolated function at the nodes is equal to the values of the unknown coefficients in the finite element representation. Schematically,

$$F(\theta, t) = \sum_{i=1}^{N} \alpha_i(t)\, L_i(\theta), \quad \psi(\theta, t) = \sum_{i=1}^{N} \beta_i(t)\, L_i(\theta), \tag{36}$$

with

$$F(\theta = \theta_i) = \alpha_i, \qquad \psi(\theta = \theta_i) = \beta_i, \tag{37}$$

where N is the number of nodes in the mesh, α_i and β_i are the unknown coefficients, and L_i are the Lagrangian basis functions. This interpolation is $\mathcal{O}(h^3)$ and $\mathcal{O}(h^2)$ accurate when representing the function and its derivative, respectively, where h is the size of an element. Moreover, it gives rise to banded matrices with bandwidths of five. This last feature, however, is of little help, when the resulting matrix must be combined with the fully populated matrix obtained from the integral equation.

The cubic *B*-splines are nonzero over four elements at most and guarantee continuity of the function along with its first and second derivatives [39]. Since $B_i(\theta = \theta_j) \neq \delta_{ij}$ the coefficients, a_i, b_i, of the *B*-spline representation

$$\begin{aligned} F(\theta, t) &= \sum_{i=0}^{N+1} a_i(t)\, B_i(\theta), \\ \psi(\theta, t) &= \sum_{i=0}^{N+1} b_i(t)\, B_i(\theta), \end{aligned} \tag{38}$$

are different from the values of the unknown functions at the nodes. Consequently, this representation will require an additional matrix multiplication in order to obtain the nodal values of the functions. The coefficients corresponding to fictitious nodes outside the domain, namely, a_0, a_{N+1}, b_0, b_{N+1}, are expressed in terms of coefficients in the interior nodes by using boundary conditions. Since *B*-splines extend over four elements, they give rise to a banded matrix with a bandwidth of seven and require more calculations for the construction of the system matrix. These small disadvantages are outweighed by the increased accuracy and smoothness of the solution. This is because *B*-splines are $\mathcal{O}(h^4)$ and $\mathcal{O}(h^3)$ accurate in interpolating a smooth function and its first derivative, respectively.

4.2. *Boundary-Element Implementation*

In the direct formulation only one additional equation needs to be discretized, namely, Eq. (20). This is done in a fashion similar to that of the differential equations previously described, and the corresponding unknown is written as either

$$\frac{\partial \Phi}{\partial n}(\theta, t) = \sum_{i=1}^{N} \delta_i(t)\, L_i(\theta) \tag{39a}$$

or

$$\frac{\partial \Phi}{\partial n}(\theta, t) = \sum_{i=0}^{N+1} d_i(t)\, B_i(\theta). \tag{39b}$$

By letting the field point approach each one of the nodal points N equations are obtained. The axisymmetric kernels G and $\partial G/\partial n$ are given in spherical coordinates as

$$G = \frac{K(m)}{\pi \sqrt{a+b}} \tag{40}$$

and

$$\begin{aligned} \frac{\partial G}{\partial n} &\equiv n_r \frac{\partial G}{\partial r} + n_\theta \frac{\partial G}{\partial \theta} \\ &= \frac{n_r}{\pi \sqrt{a+b}} \frac{1}{2F} \left[\frac{F'^2 - F^2}{a-b} E(m)\, K(m) \right] \\ &\quad + \frac{n_\theta F'}{\pi \sqrt{a+b}} \\ &\quad \times \left[\frac{4 \cos\theta \sin\theta'}{a+b} \frac{dK}{dm} - \frac{\sin(\theta+\theta')}{a-b} E(m) \right], \end{aligned} \tag{41}$$

where

$$a = F^2 + F'^2 - 2FF' \cos\theta \cos\theta' \tag{42}$$

$$b = 2FF' \sin\theta \sin\theta' \tag{43}$$

$$m = \frac{2b}{a+b}. \tag{44}$$

Also, $K(m)$ and $E(m)$ are the elliptic integrals of the first and second kind, respectively. These integrals are approximated with less than 2×10^{-8} error by the expressions

$$K(m) = \sum_{i=0}^{4} A_i m_1^i + \ln\left(\frac{1}{m_1}\right) \sum_{i=1}^{4} C_i m_1^i \tag{45}$$

$$E(m) = 1 + \sum_{i=1}^{4} D_i m_1^i + \ln\left(\frac{1}{m_1}\right) \sum_{i=1}^{4} E_i m_1^i, \tag{46}$$

where $m_1 = 1 - m$, and A_i, C_i, D_i, and E_i are constants given in [40]. When the field point (F', θ') coincides with one of the source points (F, θ), the G kernel exhibits a logarithmic singularity of the form $\ln 1/(a-b) = \ln 1/|\mathbf{x} - \mathbf{x}'|^2$, while the $\partial G/\partial n$ kernel exhibits a stronger singularity of the form $|\mathbf{x} - \mathbf{x}'|^{-1}$. The former term is integrated by resorting to a 12-point logarithmic quadrature [37]. The latter term is rendered regular by the procedure described in the previous section. The remaining regular terms are integrated using the normal Gaussian quadrature with varying numbers of Gauss points as suggested in [41]. For further details, see Pelekasis *et al.* [20].

Use of the indirect method, requires discretization of three equations, namely, Eqs. (32), (33), and (35). In particular, Eq. (35) is a differential equation and can be solved using finite elements as described for the kinematic and dynamic boundary conditions. Equations (32) and (33), however, are integral equations and are discretized in a fashion similar to that discussed for the Green's function formulation. The only new kernel is $\tilde{G}$ and is given by

$$\tilde{G}(F, \theta, F', \theta') = \left(-\frac{n_\theta}{F} + \frac{n_r}{F}\cot\theta + \frac{n_r}{r}\frac{\partial}{\partial\theta} - n_\theta \frac{\partial}{\partial r}\right) \times \left[\frac{(2-m)\,K(m) - 2E(m)}{m\pi\sqrt{a+b}}\right]. \tag{47}$$

When the field and source points coincide, $\tilde{G}$ exhibits a strong singularity ($|\mathbf{x} - \mathbf{x}'|^{-1}$), when the integration is performed along a line, and the calculation proceeds as discussed for the $\partial G/\partial n$ kernel.

Equation (32) is an integral equation of the second kind, when solved for the dipole distribution density. Thus, an iterative procedure can be used as a more efficient alternative to the direct inversion. Usually, ten iterations were sufficient for convergence of the norm $\sum_{i=1}^{N} |\mu_i^{k+1} - \mu_i^k|/N$ between iteration k and $k+1$ to less than 10^{-5}. A similar behavior was observed in [32]. However, the savings in CPU time over the direct inversion turn out to be minimal, since, for the discretization used here, almost 90% of the time is spent in constructing the system matrix and only 10% in inverting it. This is expected to change for problems of larger size. Subsequently, the vector potential $\mathbf{T}_\phi$ is calculated using Eq. (33), which amounts to a matrix multiplication.

If at most 101 nodes are used in the free surface, the direct approach is 30% faster than the indirect one. The reason is again that most of the numerical effort is consumed in constructing the system matrices rather than inverting them and in the latter approach two matrices have to be constructed per time step. Table I gives the CPU time requirements with increasing number of elements for the two integral formulations. The approaches involving direct matrix inversion and iterations until convergence are also compared in terms of CPU time, when the integral formulation of the second kind is used. The numbers quoted correspond to CPU seconds per time step on the IBM 3090 at CNSF. In all cases the computation time was found to be roughly tripled when the number of elements used was doubled.

4.3. *Integration in Time*

The kinematic and dynamic boundary conditions are used for advancing in time the location of the free surface and of the value of the surface potential, respectively. Using the Galerkin/finite-element method these equations may be written schematically

$$\mathbf{M}\frac{d\mathbf{a}}{dt} = \mathbf{F}_1, \qquad \mathbf{M}\frac{d\mathbf{b}}{dt} = \mathbf{F}_2, \tag{48}$$

where $\mathbf{M}$ is the common mass matrix and $\mathbf{F}_1$, $\mathbf{F}_2$ are the forcing vectors for the kinematic and dynamic equations, respectively. Upon inversion of the mass matrices, Eqs. (51)

TABLE I

CPU Time, in Seconds, Required per Time-Step on the IBM 3090 at CNSF for the Direct and Indirect Method, with Increasing Number of Nodal Points, N; B-Cubic Splines Are Used along with the Fourth-Order-Accurate R–K

		Indirect method	
N	Direct method	Inversion	Iterations
26	1.78	2.3	2.34
51	4.75	6.7	6.3
101	14.5	21.75	19.95

are employed with either an explicit or an implicit time-integration scheme. The fourth-order Adams–Bashforth–Moulton (A–B–M) predictor–corrector method and the fourth-order Runge–Kutta (R–K) integrator are the explicit schemes considered. First, the free boundary and the velocity potential are advanced in time. Subsequently, either one of the integral formulations is used to calculate the normal velocity at the interface. This procedure needs to be repeated once more for the corrector step in the A–B–M method and three more times for the usual intermediate steps in the R–K method. Since both algorithms are equally accurate, $\mathcal{O}(\Delta t^4)$, their stability characteristics will be the decisive factor in choosing one of the two.

If the corrector step in the A–B–M method is repeated until two consecutive solution vectors agree to within a prescribed tolerance the scheme becomes implicit. This amounts to solving a set of nonlinear algebraic equations by successive substitutions, where the predictor provides an initial guess. The scheme converges when a Lipschitz condition is satisfied. For a given spatial discretization this provides an upper limit to the time-step. The rate of convergence is linear. Each time the corrector step is repeated, the free surface and the potential are advanced and the normal velocity is found using the integral equation.

As an alternative implicit scheme, the trapezoidal rule was used with Newton's iterations to solve for all three unknown functions simultaneously. This requires inversion of a matrix that is three times the size of the matrix generated by the integral equation alone. However, the rate of convergence is now quadratic. Due to the additional number of equations involved in the indirect formulation, this method was used in conjunction with the direct formulation only. The set of the $3N$ nonlinear residual equations is written schematically as

$$\mathbf{R}(\mathbf{y}) = 0, \tag{49}$$

where,

$$\mathbf{y} = (a_1, a_2, ..., a_N, b_1, b_2, ..., b_N, d_1, d_2, ..., d_N) \tag{50}$$

is the vector of all the unknowns. Newton's method starts

[redacted]

ments to the solution vector by

$$\mathbf{y}^{k+1} = \mathbf{y}^k - \mathbf{J}^{-1}\mathbf{R}(\mathbf{y}^k), \qquad k = 0, 1, ... \tag{51}$$

The Jacobian matrix $\mathbf{J} = \partial\mathbf{R}/\partial\mathbf{y}$ is analytically calculated and is fully populated. A standard IMSL routine (DLFTRG) is used for its factorization. Typically, three to four iterations are sufficient to reduce the error in the Euclidean norm to less than 10^{-8}.

Since calculation of elements in the Jacobian matrix corresponding to the Laplacian involves differentiation of the already singular kernels G and $\partial G/\partial n$, one might expect that even stronger singularities will arise. However, as explained in [20], this is not true, since at the singular point G and $\partial G/\partial n$ depend on the coefficient y_i both through F and F'. As a result, the strongly singular terms cancel each other out and the Jacobian elements exhibit the same type of singular behavior as the residual equations.

No unstable eigenmodes exist for the linear problem under examination [28]. However, free-surface inviscid flows are known to be subject to instabilities due to discretization error in the dispersion relation that may cause resonance between modes [4, 14, 32]. These instabilities are not associated only with explicit integration schemes in which case they would be removable by reducing the time-step (conditional stability). Instead, they are identified by the growth of the mode containing as many waves as allowed by the number of nodal points. For instance, when 101 nodal points are used, the Legendre mode P_{100} is growing faster than any other mode. This is a nonlinear instability because it is accelerated when the initial disturbance amplitude is increased. Finer discretization in space excites the new highest mode captured and along with temporal refinement simply postpones the instability without ever eradicating it [21].

The high-mode instability has been observed in the present study also and mainly in the indirect formulation. With that formulation, introduction of artificial viscosity (filtering) is necessary in order to damp out the higher modes while leaving the lower ones essentially unaffected. When Green's theorem is used, filtering is ineffective because the highest modes do not grow as fast. The filtering scheme employed in [32] is also used here. In particular, after each time-step the surface potential is smoothed out by

$$\frac{\partial\psi}{\partial t} = \lambda\frac{\partial^4\psi}{\partial\theta^4}. \tag{52}$$

Equation (52) is approximated by a second-order-accurate formula for the fourth derivative and an Euler time-step, giving

[redacted]

Specific values for the time-step, number of elements, and the remaining parameters used in the calculation are given in the next section. In all cases, time-steps selected were so small that, considering the increased accuracy characteristics provided by the fourth-order-accurate R–K or A–B–M time integrators, numerical error was controlled by spatial discretization. Consequently, evaluation of spatial derivatives of the shape-function and surface potential were the error-controlling factors resulting in $\mathcal{O}(h^2)$- and $\mathcal{O}(h^3)$-

accurate numerical schemes for quadratic basis functions and cubic B-splines, respectively. This behavior persisted until the accuracy of the results was significantly reduced due to growth of high modes. At any rate, shapes were calculated accurately to at least two significant digits. Global accuracy was guaranteed by monitoring the invariants of the motion.

Table II compares the performance of the direct method with increasing number of elements at three different locations on the free surface at time $t = 6.72$, corresponding to approximately eight periods of P_4. The fourth Legendre mode was excited initially and the amplitude, ε, was set to 0.3. A time-step of 0.001 was used when 100 elements were taken on the free surface, whereas the time-step was set to 0.002 with both 25 and 50 elements. The fourth-order-accurate R–K time integrator was employed along with B-cubic splines. As expected, accuracy is not as good at the pole, $\theta = 0$, where the solution is captured up to the second significant digit. Away from the pole, e.g., at the equator, $\theta = \pi/2$, and at intermediate points, $\theta = 0.754$, solution is captured up to the third significant digit. Convergence of the method conforms well with the aforementioned $\mathcal{O}(h^3)$ behavior for the numerical error in the location of the boundary. Practically, this behavior implies that doubling of the number of elements improves the solution for the unknown function by one significant digit; see Table II. Note that the solution at the pole also behaves in this way, even though it is less accurate in general.

The solution obtained with the indirect formulation converges at the same rate provided that short waves have not evolved yet. In the above table, values for the location of the free surface are given, obtained with the indirect formulation and calculated at the same time and meridianal position as the ones given for the direct formulation. The same space and time discretization schemes were used as with the direct formulation. The time step Δt was set to 0.002, while 101 nodes were used on the free surface and the filtering parameter $\lambda \Delta t = -0.004$. Agreement with the direct formulation is obvious. As time increases however, short waves grow significantly and results obtained with the indirect formulation become inaccurate.

TABLE II

Convergence with Increasing Number of Nodal Points, N, of the Boundary Location at the Pole, $\theta = 0$, the Equator, $\theta = \pi/2$, and an Intermediate Point, $\theta = 0.754$; $\varepsilon = 0.3$, $n = 4$, $t = 6.72$

	Direct method			Indirect method
θ	$N = 26$	$N = 51$	$N = 101$	$N = 101$
0.0	1.3869	1.3435	1.3541	1.3549
0.754	0.88297	0.8962	0.8986	0.8976
1.571	1.0602	1.06297	1.0668	1.0637

5. RESULTS AND DISCUSSION

5.1. *Linear Oscillations*

Capillary oscillations of a liquid drop for infinitesimal disturbances were examined by Rayleigh [26], who calculated the dimensionless frequency for each linear mode, k,

$$\omega_k = \sqrt{k(k-1)(k+2)}. \tag{54}$$

Numerical solution of the linear problem is very simple since the discretized equations are also linear and can be solved by a single matrix inversion, even when an implicit scheme is used [43]. Furthermore, with a constant time-step, the system matrix remains constant and needs to be inverted only once. The time-stepping algorithm is constructed by multiplying the inverted matrix with the updated right-hand-side vector. Thus, large savings are achieved in computer time which is not significantly increased when the time-steps are decreased. As a result, a simple implicit integration scheme, like the trapezoidal rule (TR), is preferable because of its stability characteristics.

Oscillations of a liquid drop induced by an initial excitation of the fourth Legendre mode were computed. First, the direct formulation was used with 50 quadratic Lagrangian elements and a time step $\Delta t = T_4/200$, where $T_4 = 2\pi/\omega_4 = 0.7405$ is the period of the four-lobed mode as predicted by the linear theory. Integration in time was carried out for 10 periods and required 181 CPU sec on an IBM 3084 machine. The results at the end of computations were

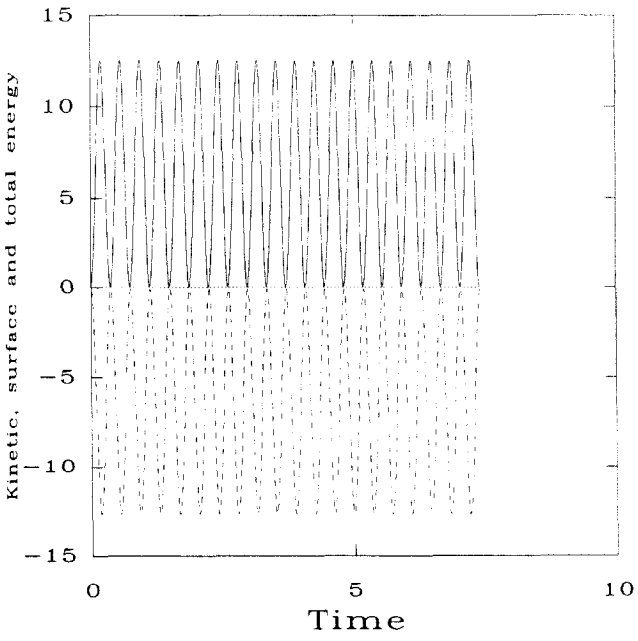

FIG. 1. Linear oscillation of kinetic (—), surface (– – –), and total energy (···) during several periods of the four-lobed mode. The surface energy has been translated so that it starts from zero.

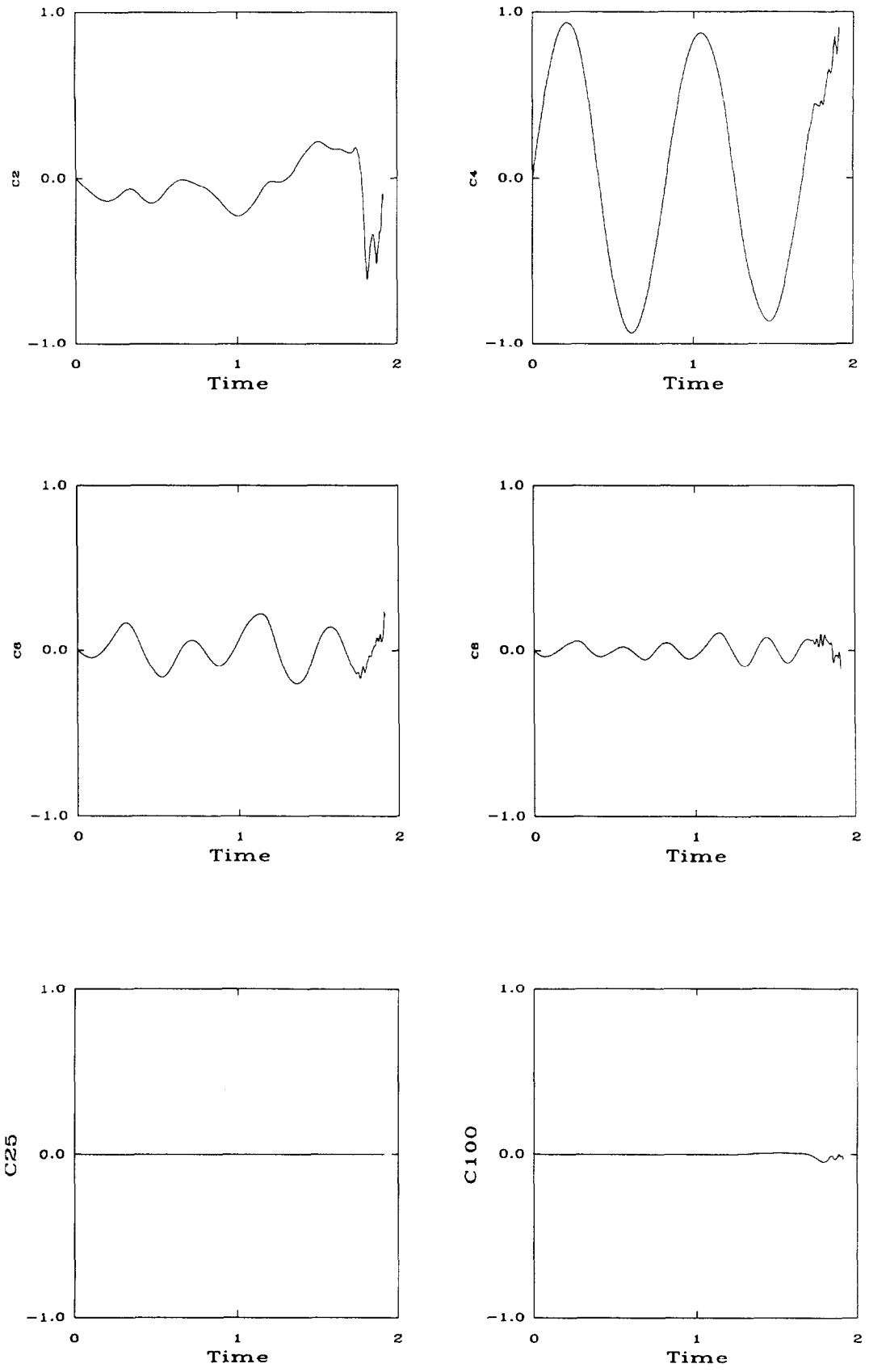

FIG. 2. Variation of the Legendre coefficients, c_i, of the velocity potential normalized with the linear amplitude of P_4. Indirect method and B-splines were used; $\varepsilon = 0.3$, $N = 101$, $\Delta t = 0.002$, $\lambda = 0$.

TABLE III

Performance of Indirect Formulation with Cubic *B*-Splines and Fourth-Order R–K

Number of nodes	Time step Δt	Filtering $\lambda \Delta t$	Variation of total energy
51	0.008	None	Immediate exponential increase
51	0.004	None	Increases by 6% after two periods of P_4
51	0.002	None	Increases by 0.1% after two periods of P_4
51	0.004	−0.004	Decreases by 0.09% after two periods of P_4 and by 0.27% after five periods of P_4
51	0.004	−0.002	Decreases by 0.05% after two periods of P_4
51	0.004	−0.001	Decreases by 0.03% after two periods of P_4
101	0.004	None	Immediate exponential increase
101	0.002	None	Increases by 0.0004% after one period of P_4
101	0.002	−0.005	Decreases by 0.0064% after one period of P_4
101	0.002	−0.004	Decreases by 0.002% after eight periods of P_4, but more so after nine periods
101	0.002	−0.002	Decreases by 0.018% after four periods of P_4, but increases after five periods

accurate to three significant digits for the drop shape as well as for the potential and to two significant digits for the normal velocity. The total energy and mass flux were conserved with an accuracy of five significant digits. There is a slight decrease in accuracy with time, probably due to interactions of the primary mode with higher ones that are introduced due to round-off error. The distance between consecutive maxima in the oscillations of the normalized fourth Legendre mode, provides the period of its oscillation, $T_4 = 0.740$, accurately to three significant digits. The period

TABLE IV

Performance of Direct Formulation with the Fourth-Order Explicit/Implicit A–B–M Method and the Fourth-Order Explicit R–K Method and Both Types of Basis Functions

A–B–M		R–K	
Number node	Maximum time step for convergence of iterations/stability	Number of nodes	Maximum time step for stability
21	0.0025	51	0.004
41	0.001	101	0.001
81	0.00025		

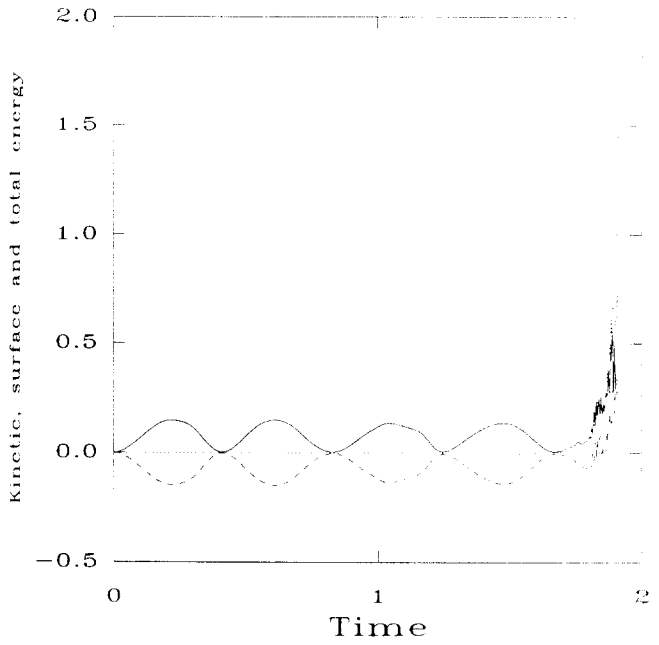

FIG. 3. Variation of kinetic (—), surface (− − −), and total energy (···). Indirect method and *B*-splines were used; $\varepsilon = 0.3$, $N = 101$, $\Delta t = 0.002$, $\lambda = 0$. The surface energy has been translated so that it starts from zero.

of oscillation of the kinetic and surface energy is measured from Fig. 1 and it is exactly one-half of T_4, as expected [28]. In this and all subsequent plots showing variation of the energy of the system, it should be understood that the surface energy is normalized to zero.

Subsequently, the indirect formulation was used and

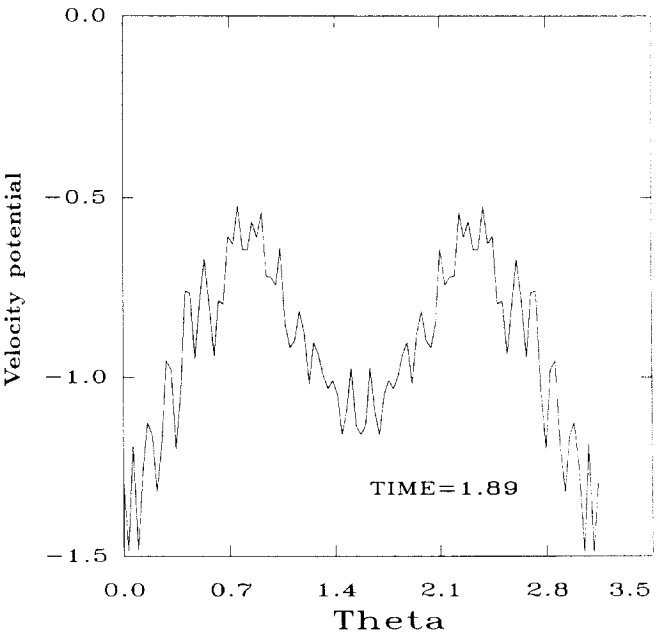

Fig. 4. Profile of velocity potential obtained with the indirect method and *B*-splines at $t = 1.89$; $\varepsilon = 0.3$, $\Delta t = 0.002$, $\lambda = 0$.

yielded similar results. Introduction of cubic B-splines significantly improved accuracy over the Lagrangian basis integration for very long time intervals. Unless otherwise indicated, the mode that is initially excited is the four-lobed slight increase in the required CPU time, but it is more than compensated for by the higher accuracy and smoothness of the solution.

5.2. *Nonlinear Oscillations*

Important nonlinear effects in the present and similar problems in drop dynamics [21, 28, 32, 42] evolve very slowly in time, e.g., after several periods of the primary oscillation. Thus, the major goal of the present analysis is to provide a robust numerical scheme for accurate and efficient

5.2.1. *Indirect Formulation with Lagrangian Basis Functions.* It is found that representing dependent variables via Lagrangian quadratic basis functions is much less accurate than via cubic B-splines for the same numerical effort. This is generally true for both direct and indirect formulations. In particular, when the indirect formulation with Lagrangian basis functions is used the resulting scheme fails irrespective of the time integrator. Total energy increases and higher modes show abnormal increase in amplitude even before half a period of the primary oscillation is

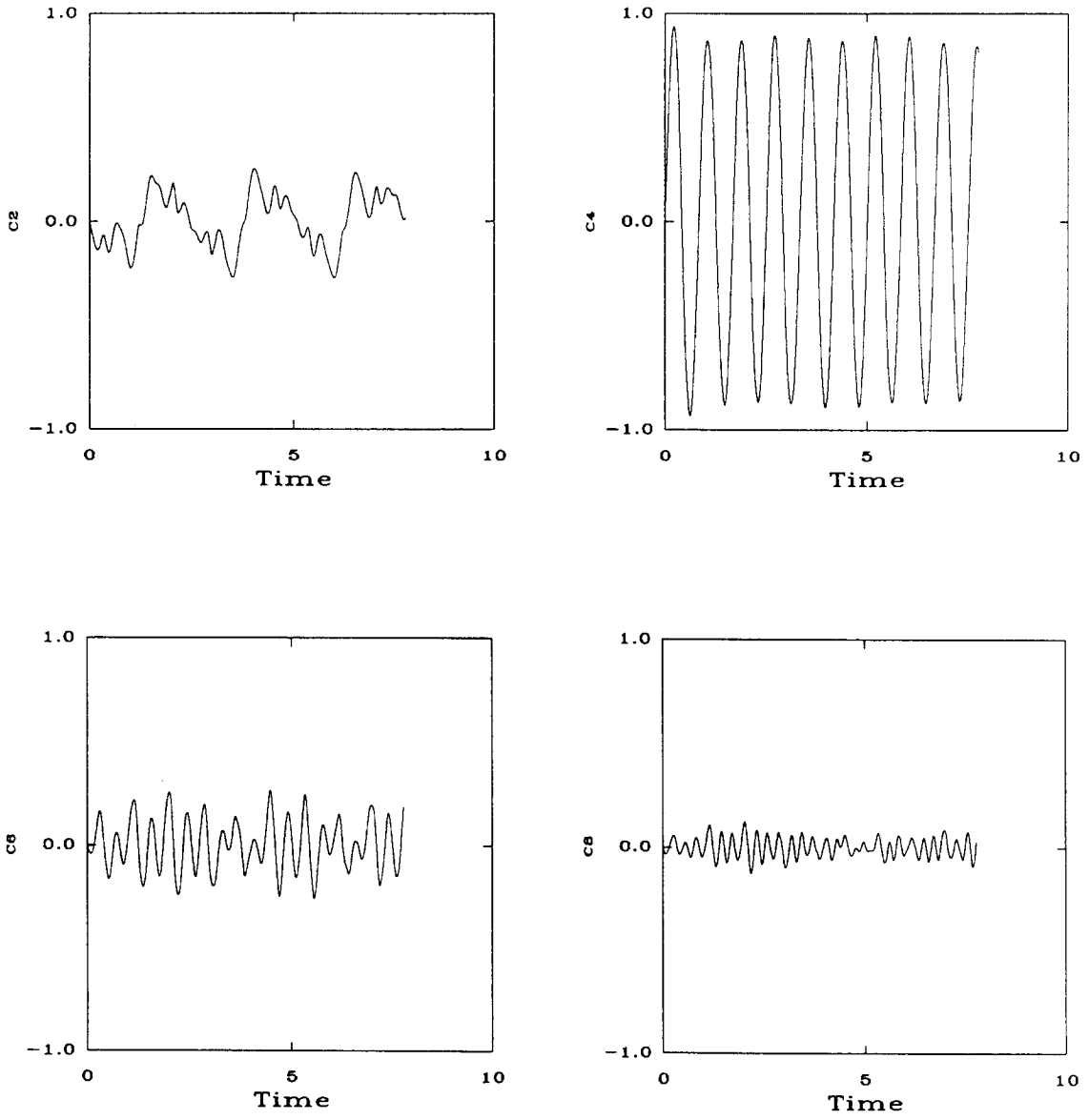

Fig. 5. Variation of the Legendre coefficients, c_i, of the velocity potential normalized with the linear amplitude of P_4. Indirect method and B-splines were used; $\varepsilon = 0.3$, $N = 101$, $\Delta t = 0.002$, $\lambda \Delta t = -0.004$.

reached. Reduction of the time-step size does not improve the situation. Mesh refinement only shifts the problem to higher modes. For example, use of 101 nodal points excites the modes closer to P_{100}. By increasing the disturbance amplitude these modes grow even faster. Use of filtering cannot remedy the situation due to the very high growth rates of the short waves. This instability is, most likely, due to inaccuracies in calculating derivatives of dependent variables using the Lagrangian basis functions.

5.2.2. *Indirect Formulation with Cubic B-Splines.* In an effort to eliminate the aforementioned instability cubic *B*-splines are introduced. They are expected to enhance smoothness of the solution since they guarantee continuity of the first and second derivatives of the dependent variables. The Runge–Kutta integrator is used, since it exhibited slower short-wave growth even with Lagrangian basis functions. This method is quite similar to the one employed in [32] except that a Lagrangian (as opposed to Eulerian) approach and fourth order accurate Padé approximate formulas for spatial discretization were employed there.

Table III shows that, although *B*-splines reduce the growth rate of high modes, they require numerical filtering in order to integrate for longer times. More specifically, when 101 nodes are used with $\Delta t = 0.004$ there is an exponential growth of all modes and the energy, probably due to the unsatisfied stability requirements of R–K.

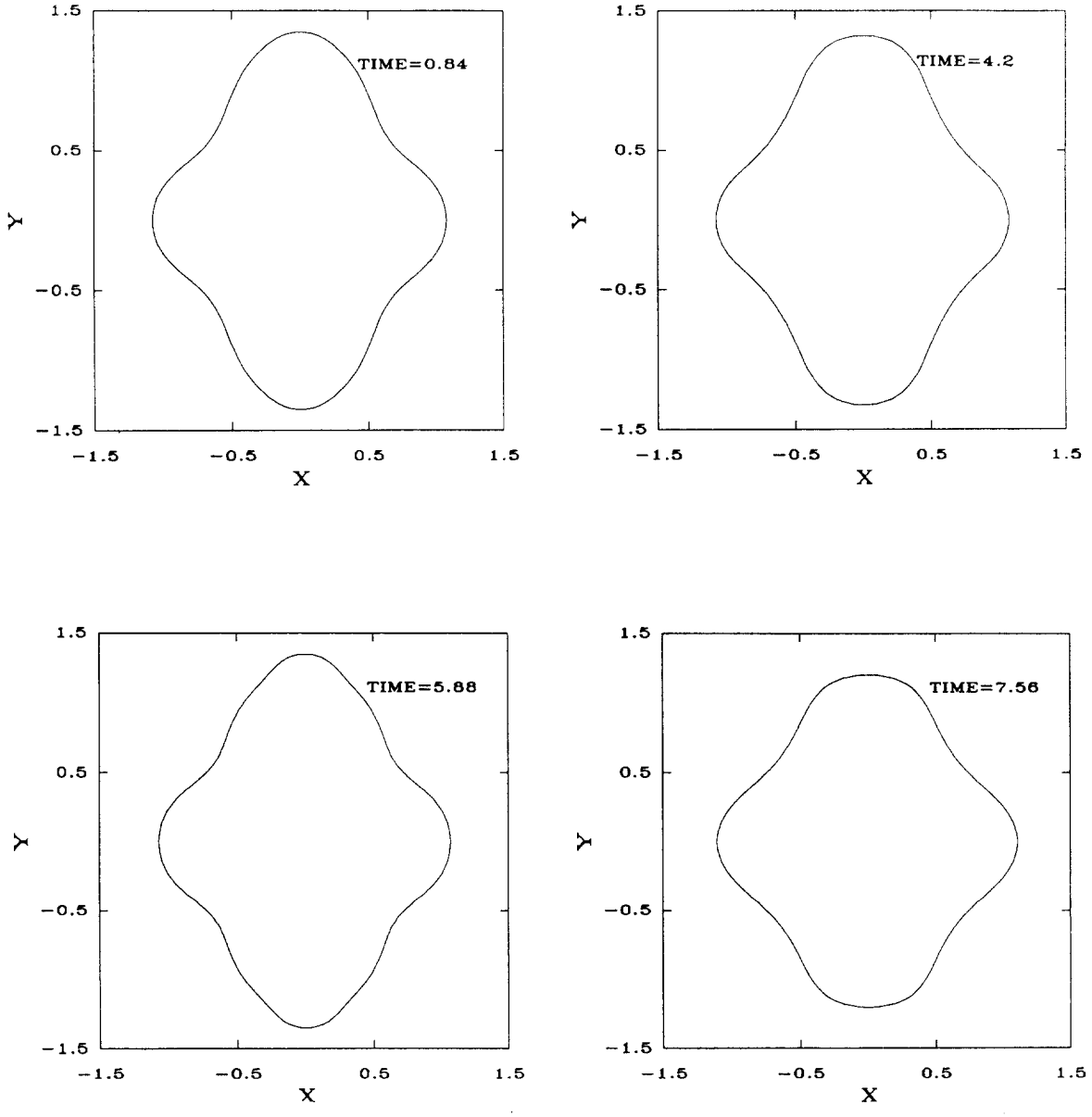

Fig. 6. Evolution of drop shapes using the indirect method and cubic *B*-splines, $\varepsilon = 0.3$, $N = 101$, $\Delta t = 0.002$, $\lambda\, \Delta t = -0.004$.

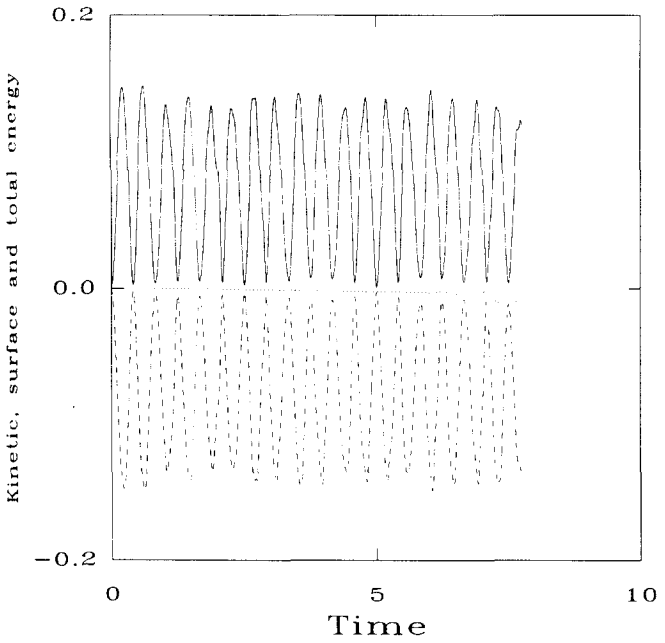

FIG. 7. Evolution of kinetic (—), surface, (– – –), and total energy (···) over nine periods of P_4 with indirect method; $\varepsilon = 0.3$, $N = 101$, $\Delta t = 0.002$, $\lambda \Delta t = -0.004$. The surface energy has been translated so that it starts from zero.

A smaller time-step, $\Delta t = 0.002$, eliminates this instability but still allows for slow growth of high modes and energy. Figure 2 shows the evolution of several Legendre coefficients of the potential, P_2, P_4, P_6, P_8, P_{25}, and P_{100}, prior to the application of numerical viscosity ($\lambda = 0$). The higher modes, P_{50}, P_{98}, P_{100}, grow faster than the intermediate ones, P_{20}, P_{25}, P_{30}; see [45]. The evolution of P_{25} and P_{100} is indicative of the general trend. The same behavior is observed for the normal velocity and drop shape, but it is less pronounced. Figure 3 shows the increase in energy after two periods of oscillation of P_4 also. The distribution of velocity potential around the drop surface after two periods of oscillation is shown in Fig. 4. Note the loss of smoothness, especially close to the poles. This is commonly observed in simulations of axisymmetric potential flows [18, 32] and is attributed to rapid variation of the elliptic integrals between nodes near the poles. Furthermore, as the number of nodes is increased the loss of accuracy at the poles decreases, see also Table II.

When filtering is applied with $\lambda \Delta t = -0.002$, a slight decrease in energy and the physically expected growth of higher modes are observed after four periods of oscillation. Subsequently, the energy increases monotonically.

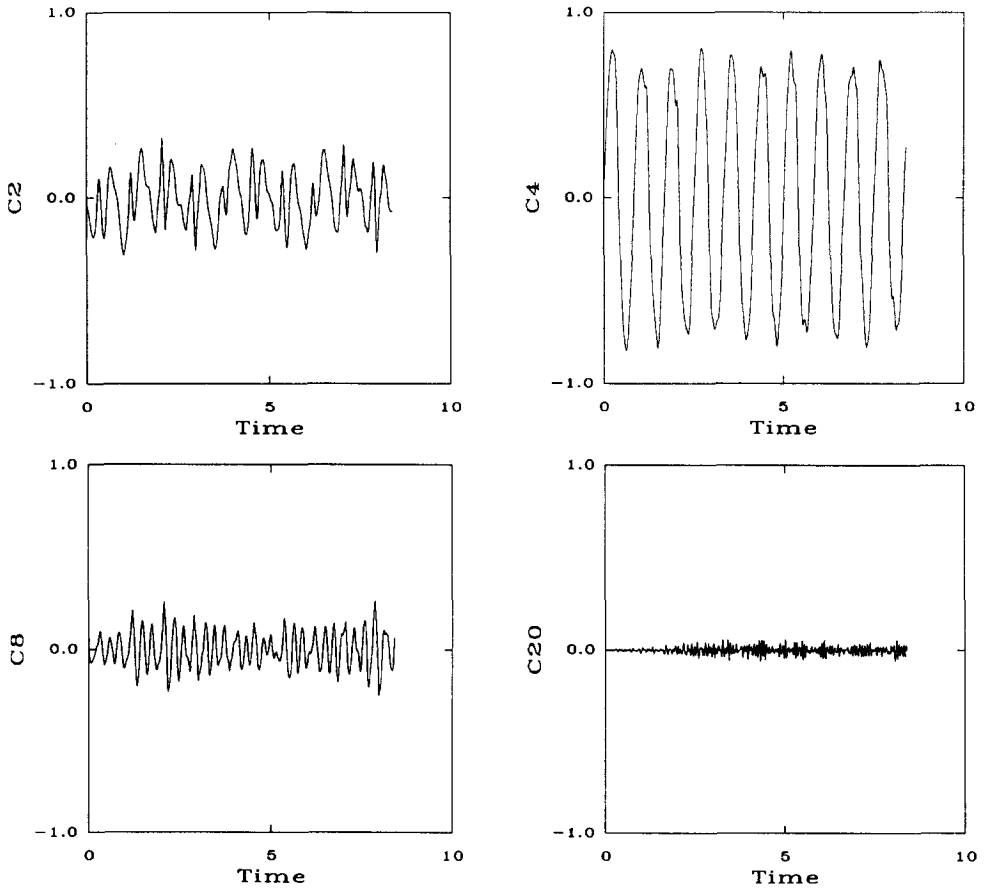

FIG. 8. Variation of the normalized Legendre modes of the normal velocity at the drop surface obtained with the direct method and *B*-splines; $\varepsilon = 0.3$, $N = 101$, $\Delta t = 0.001$, $\lambda = 0$.

Doubling of the filtering parameter to $\lambda\,\Delta t = -0.004$ allows integration to proceed for about eight periods. At that point energy decreases drastically for a short time and eventually increases exponentially. Lundgren and Mansour [32] used an even larger parameter for filtering and integrated for about 20 periods of P_4 with $\Delta t = 0.005$, observing a somewhat larger decrease in energy. This is in agreement with the trend observed here. Figure 5 shows the evolution of the first four Legendre modes of the potential over eight periods of P_4. The high modes, e.g., P_{50}, P_{98}, P_{100}, have been successfully damped and are not shown, see [45].

A closer examination of the lower modes, P_2, P_4, P_6, P_8, reveals interesting coupling phenomena which are similar to those observed and analyzed by others. A second beat is superimposed on the expected slower oscillations of the two-lobed mode, with roughly half the period of P_4, as a result of nonlinear coupling [28]. There is also a slow beat between the fourth and the sixth modes indicating resonance [32, 42]. Even though the linear periods are $T_4 = 0.7405$ and $T_6 = 0.4056$, the numerical values of their nonlinear counterparts are larger (as expected [28]) and such that $T_4 = 0.84$ is almost twice as large as $T_6 = 0.43$. This favors second-order resonant coupling between the two modes [42]. The eighth mode is excited through second-order coupling with the fourth mode [28], but as time increases resonant envelopes arise and valleys occur very close to the crests of the P_4 envelope. Considering that

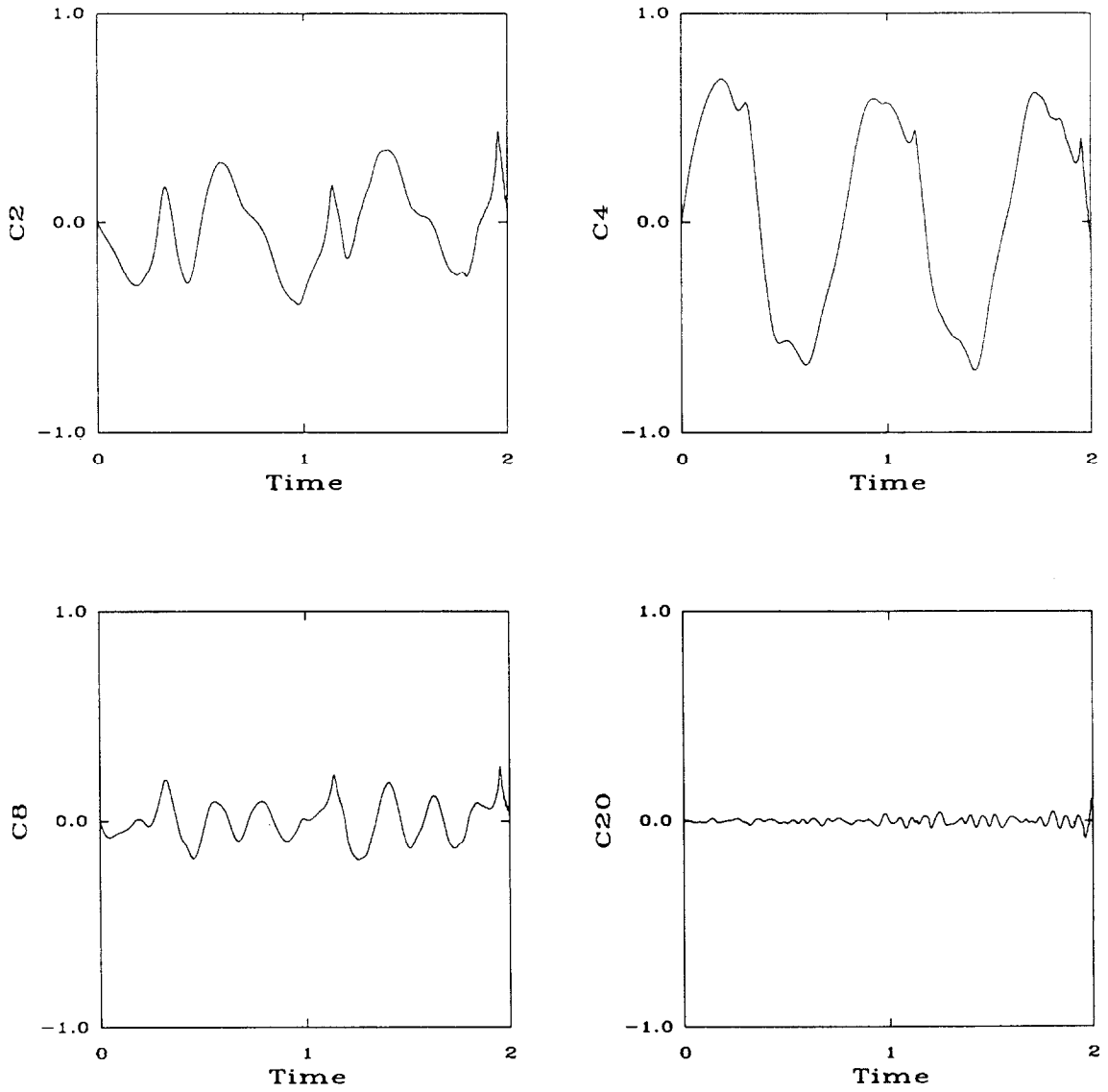

FIG. 9. Variation of the normalized Legendre modes of the normal velocity at the drop surface obtained with the direct method and *B*-splines; $\varepsilon = 0.4$, $N = 101$, $\Delta t = 0.001$, $\lambda = 0$.

the nonlinear frequency of P_4 is almost three times as large as the one of P_8, $T_8 = 0.3$, third-order harmonic resonance should be possible.

Selected drop shapes are shown in Fig. 6 obtained approximately at the end of the first, fifth, seventh and ninth period of P_4; further shapes are given in [45]. The total energy remains constant up to three significant digits and for eight periods of oscillation. Subsequently, it decreases [illegible] expected, kinetic and surface energy oscillate with half the period of P_4. In general, the drop volume is conserved more accurately than the total energy.

5.2.3. *Direct Formulation with Lagrangian Basis Functions.* This scheme does not suffer from as severe a short-wave instability as observed in the indirect method. Integration can proceed for large enough times and meaningful comparisons of different time-integrators can be performed. With explicit time integration schemes, mesh refinement requires concurrent reduction of time step in order to achieve conditional stability. As can be seen from Table IV, the fourth-order R–K method permits four times as large a time-step as the one permitted by the fourth-order A–B–M. Thus, even though R–K requires twice as many operations per time-step, it is still preferable over A–B–M. When the corrector step in A–B–M is repeated until convergence it becomes an implicit method and given the number of nodes a Lipschitz condition exists [44] that determines the maximum possible time-step for the iterations to converge. It is found here that this maximum time-step is essentially the same as the maximum time-step for numerical stability of the explicit A–B–M. Since more than one iteration is required per time-step, the implicit A–B–M is more time consuming than its explicit counterpart. Even when stability criteria are met and iterations converge, short-wave instabilities reduce the accuracy of calculations.

5.2.4. *Direct Formulation with Cubic B-Splines.* The [illegible] more easily capture a solution that varies in smaller and smaller length scales as time increases. Therefore, the appearance of high modes is significantly delayed and accurate time integration is performed for long times without resorting to filtering. Stability characteristics of the two explicit schemes were not affected by the introduction of these basis functions and made the R–K scheme the obvious choice.

For completeness, the second-order-accurate trapezoidal rule is also used and is coupled with Newton's iterations for simultaneous calculation of all the unknowns. As a result the integral equation cannot be classified either as first or second kind. The initial guess is provided by the second-order A–B formula. In order to compensate for the inversion of a matrix three times larger that arises in this method and to compare it with R–K for the same numerical effort a larger time-step must be used, $\Delta t = 0.002$ with 101 nodes. Instead, a time-step of 0.001 is used here for the same number of nodes and the direct formulation. Numerical effort is measured in terms of CPU time here, since storage requirements are limited for the relatively small number of

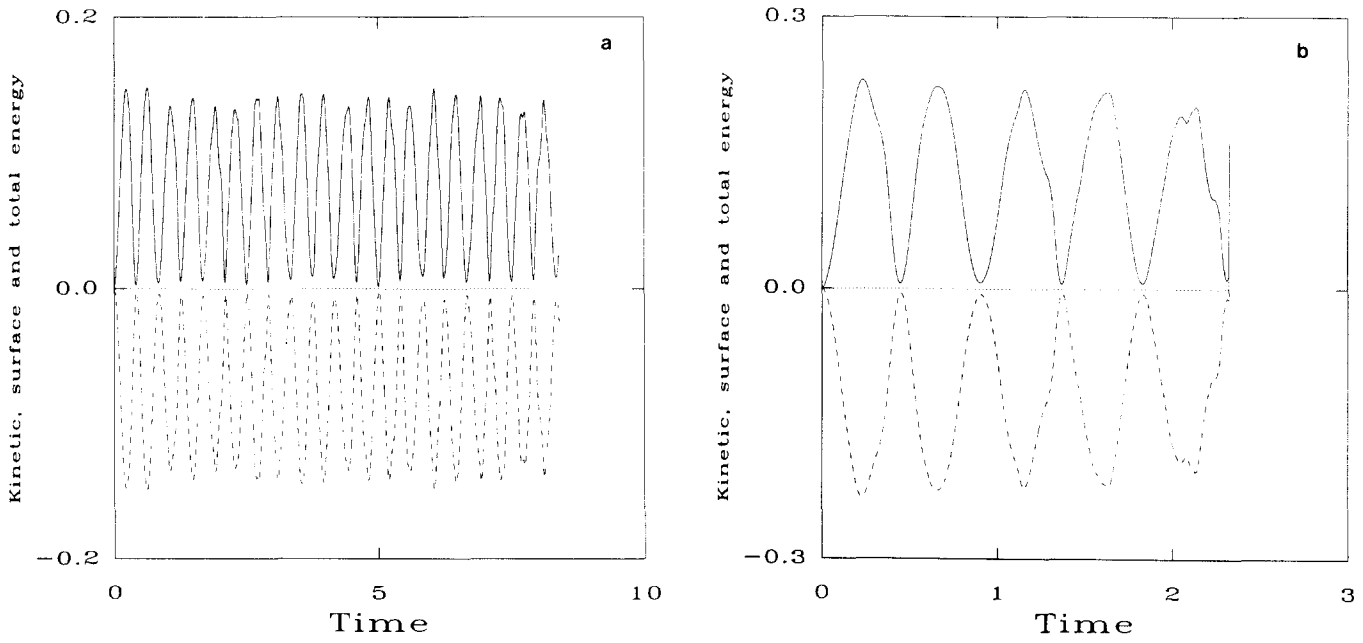

FIG. 10. Evolution of kinetic (—), surface (– – –), and total energy (···) by the direct method and *B*-splines for either (a) $\varepsilon = 0.3$ or (b) $\varepsilon = 0.4$. Surface energy has been translated so that it starts from zero; $N = 101$, $\Delta t = 0.001$, $\lambda = 0$.

unknowns used. As the number of nodes increases the system matrix constructed when the trapezoidal rule is used has to be stored out of core, which significantly reduces efficiency of the calculations. Accuracy is still controlled by the spatial discretization. Therefore, very similar results were obtained and especially for the shape they agreed to within four significant digits after four periods of P_4. The energy, however, is conserved to within six digits by R–K as opposed to five digits by the trapezoidal rule. In view of its efficiency and simpler implementation the R–K integrator is used in the remaining tests.

Figures 8 and 9 show the evolution of selected Legendre modes of the normal velocity normalized with respect to the linear amplitude of P_4 and for two different values of the disturbance amplitude, $\varepsilon = 0.3, 0.4$, respectively. The normal velocity is the most sensitive variable to short-wave instabilities in the direct formulation. Additional modes are given in [45]. When $\varepsilon = 0.3$, the intermediate modes, P_{18}, P_{20}, P_{30} exhibit a physical and gradual growth, whereas the higher modes, P_{50} and P_{100}, have not been excited. The evolution of P_2, P_4, P_8, and P_{20} is given here and is indicative of the above-described behavior. Hence integration advances for 10 periods of the primary mode with acceptable accuracy. However, when $\varepsilon = 0.4$ a more prominent increase of the intermediate modes is observed within only 2.5 periods of P_4. The high modes grow more slowly here than high modes in the indirect formulation and intermediate ones in the present formulation, hence filtering is ineffective. Figures 10a and 10b show the energy evolution for the same two cases. When $\varepsilon = 0.3$, the total energy is conserved, whereas when $\varepsilon = 0.4$, a slight increase in energy accompanies the appearance of high modes.

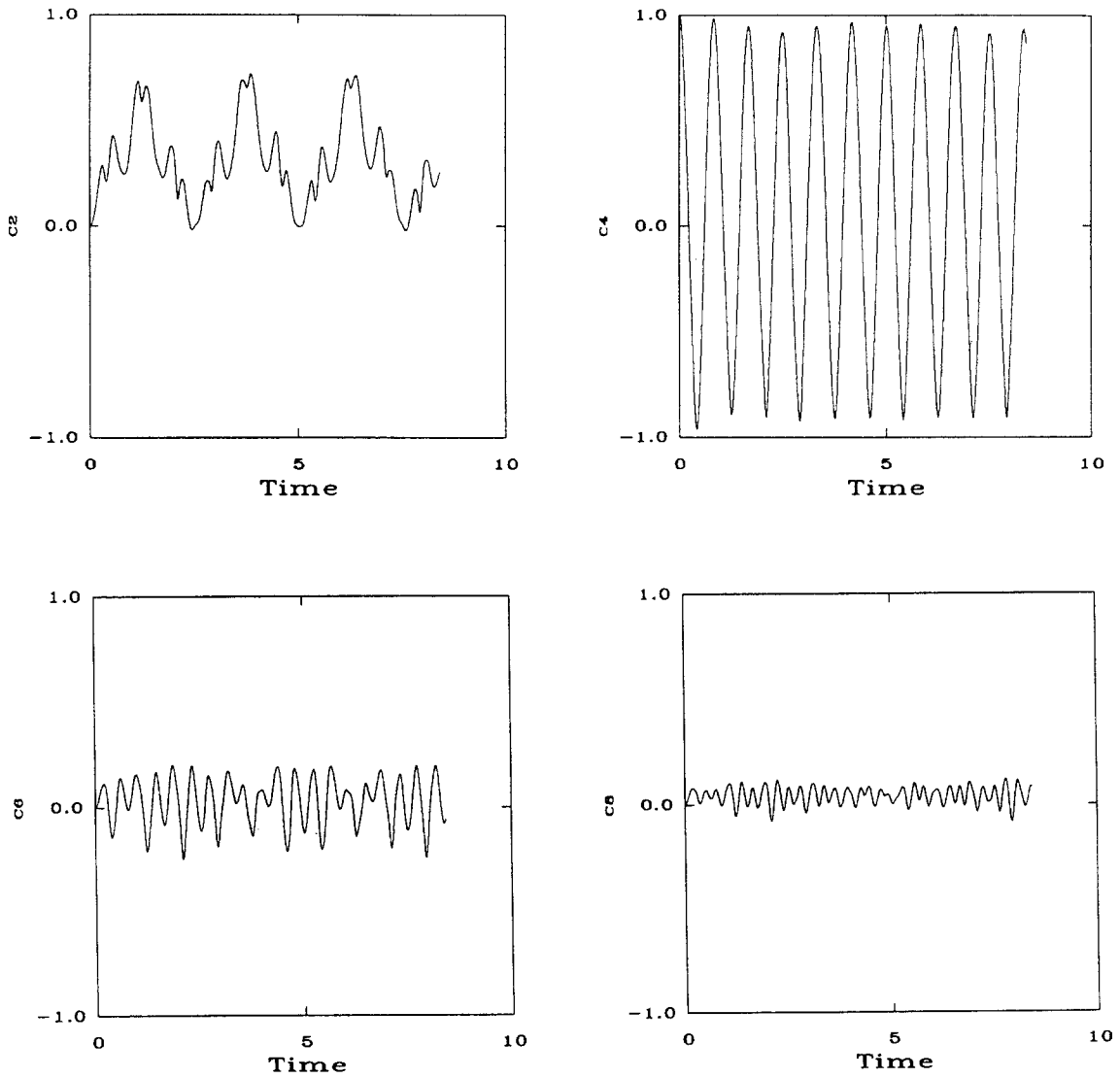

FIG. 11. Oscillations of the normalized Legendre coefficients of the drop shape obtained with the direct method and *B*-splines, $\varepsilon = 0.3$, $N = 101$, $\Delta t = 0.001$, $\lambda = 0$.

Repeating the calculations for $\varepsilon = 0.3$, but with 51 nodal points and $\Delta t = 0.002$, over the same time interval gives results that agree very well with the earlier ones. For example, energy is now conserved up to four significant digits, whereas it was conserved up to five significant digits with $N = 101$. Moreover, drop shapes, after 10 periods of the primary mode, agree up to the third significant digit except at the poles, where they agree up to two digits. As a result, short-wave growth can be treated by mesh refinement alone, when the direct formulation is used. Further comparison of solutions for the two different mesh sizes is given in Pelekasis [45]. The calculated drop shapes agree well with those calculated by the indirect method [45]. The same progressive increase of higher modes was observed. It should be noted that the motion is not strictly periodic.

The nonlinear periods of the lower Legendre modes are found by measuring the distance between successive maxima or minima in the oscillation of the corresponding coefficients shown in Fig. 11. These are the coefficients of the Fourier–Legendre decomposition of the shape function. The values obtained for P_4 are $T_4 = 0.83$ and 0.912 when $\varepsilon = 0.3$ and 0.4, respectively. Tsamopoulos and Brown [28], in their weakly nonlinear analysis, predict a decrease in the oscillation frequency with the square of the amplitude ε. In particular, the above investigators predict for the fourth Legendre mode

$$\omega_4 = \omega_{4,0}\left(1 - \frac{\varepsilon^2}{2} 2.91361\right) + \mathcal{O}(\varepsilon^4), \tag{55}$$

where ω and $\omega_{4,0}$ denote the linear and nonlinear frequency, respectively. A graphic representation of the above equation

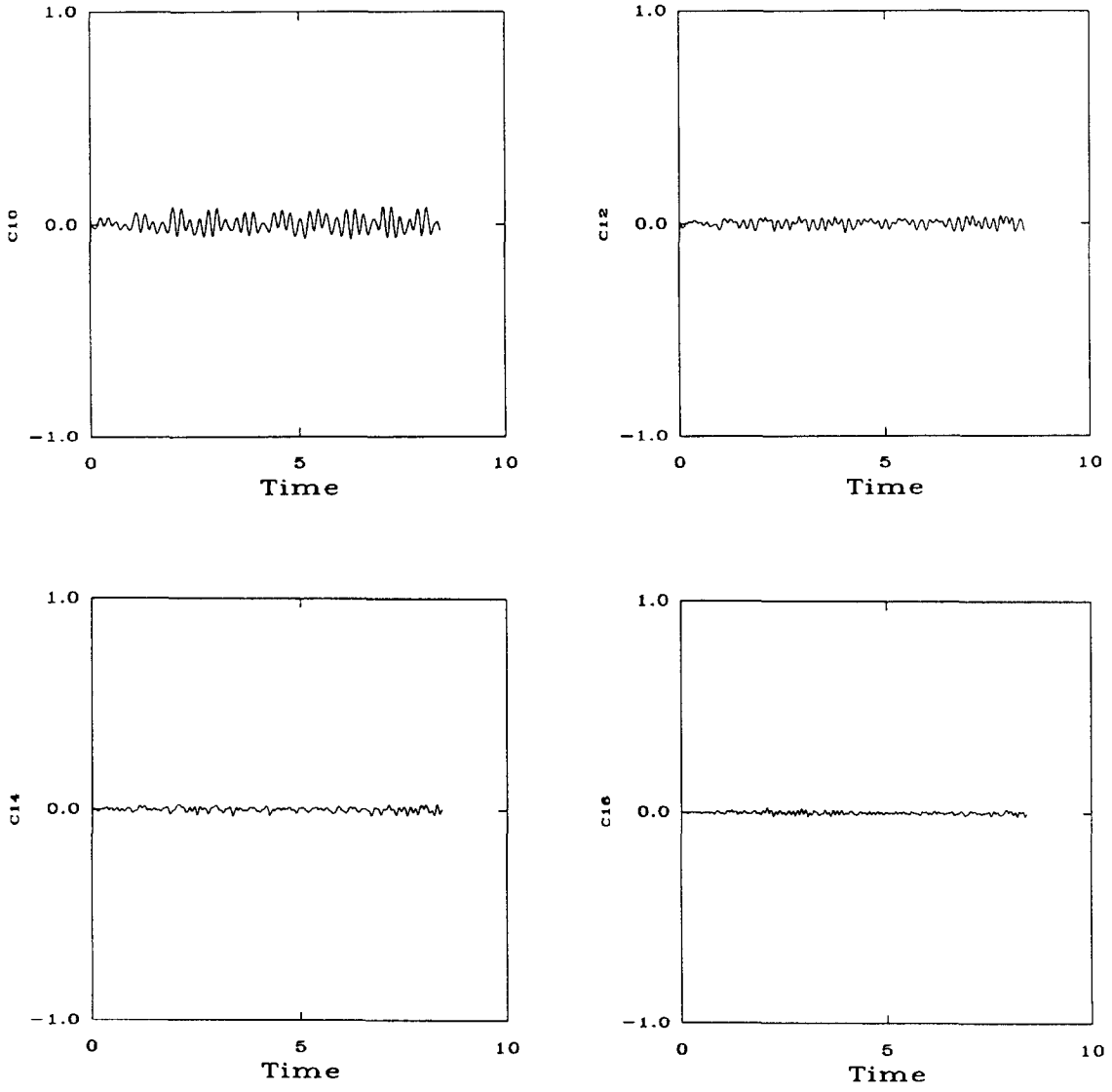

FIG. 11—*Continued*

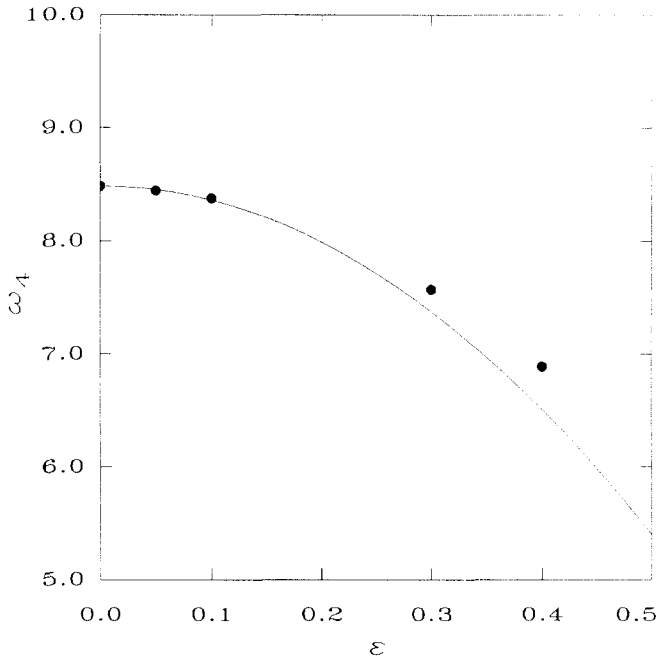

FIG. 12. Variation of the frequency of the fourth Legendre mode with increasing amplitude of the initial distortion mode, P_4, as predicted in [28]. The dots correspond to numerical results.

is given in Fig. 12. The dots correspond to numerically obtained values for the nonlinear frequency of P_4 for five different values of the amplitde, $\varepsilon = 0$, 0.05, 0.1, 0.3, 0.4. The frequencies obtained for small values of ε, $\omega_4 = 8.445$ and 8.377 when $\varepsilon = 0.05$ and 0.1, conform well with the asymptotic behavior predicted by Eq. (55). As it is generally true with asymptotic results, however, they gradually lose [illegible] numerical results for the frequency when $\varepsilon = 0.3$, 0.4 lie above the continuous curve in Fig. 12.

6. CONCLUSIONS

A hybrid finite-boundary element method for solving free-surface potential flows has been developed. The nonlinear oscillations of an inviscid liquid drop were studied as a test problem for which asymptotic solutions exist.

It was found that among the schemes tested, cubic *B*-splines and the fourth-order R–K integrator should be preferred for space and time discretization, respectively. The direct formulation that results in an integral equation of the first kind was found to prevent short-wave instabilities by mesh and temporal refinement alone and without resorting to any form of filtering. Moreover, the direct formulation consumed less CPU time per time-step than the indirect, since the latter one requires construction of one more system matrix. Filtering was necessary with the indirect method, which involves solution of an integral equation of the second kind. This is, of course, at the expense of a certain loss of accuracy, especially for long time calculations. However, filtering allows for a larger time-step. It should be anticipated that when much larger system matrices are created, their direct inversion would be the time-limiting step in the numerical algorithm.

Linear solutions and eigenfrequencies of the test problem were easily recovered. In the nonlinear regime, the motion is decelerated due to increased inertia, and nonlinear frequencies and mode coupling were calculated. Accurate calculations were performed for a long period of time. This method has been applied in studying nonlinear oscillations of a spherical liquid shell [21] and the relative motion of interacting bubbles in liquids [45], [46].

ACKNOWLEDGMENTS

This research was supported by the Fluid Mechanics Program of the National Science Foundation under Grant MSM-8705735. Usage of the Cornell National Supercomputer Facilities (CNSF) is gratefully acknowledged.

REFERENCES

1. I. Fredholm, *Acta Math.* **27**, 365 (1903).
2. O. D. Kellogg, *Foundations of Potential Theory* (Dover, New York, 1953).
3. M. A. Jaswon and G. T. Symm, *Integral Equation Methods in Potential Theory and Elastostatics* (Academic Press, New York, 1977).
4. M. S. Longuet-Higgins and E. D. Cokelet, *Proc. R. Soc. London Ser. A* **350**, 1 (1976).
5. S. T. Grilli, J. Skourup, and I. A. Svendsen, in *Proceedings 10th International Conference on Boundary Elements, Southampton, England* Publication, Springer, New York, 1988), p. 549.
6. J. W. Dold and D. H. Peregrine, in *Proceedings 19th International Conference on Coastal Engineering, Houston*, edited by B. L. Edge, 1984, p. 955.
7. D. G. Dommermuth and D. K. P. Yue, *J. Fluid Mech.* **178**, 195 (1987).
8. J. R. Blake, B. B. Taib, and G. Doherty, *J. Fluid Mech.* **170**, 479 (1986).
9. J. R. Blake, B. B. Taib, and G. Doherty, *J. Fluid Mech.* **181**, 197 (1987).
10. L. Rosenhead, *Proc. R. Soc. London Ser. A* **134**, 170 (1931).
11. G. Birkhoff, in *Proceedings of Symposia in Applied Mathematics*, Vol. 13, edited by G. Birkhoff *et al.* (American Mathematical Society, Providence, RI, 1962), p. 55.
12. D. I. Pullin, *J. Fluid Mech.* **119**, 507 (1982).
13. R. Krasny, *J. Fluid Mech.* **167**, 65 (1986).
14. D. W. Moore, *SIAM J. Sci. Stat. Comput.* **2**, 65 (1981).
15. G. R. Baker, D. I. Meiron, and S. A. Orszag, *J. Fluid Mech.* **123**, 477 (1982).
16. G. R. Baker, D. I. Meiron, and S. A. Orszag, *Phys. Fluids* **23**, 1485 (1980).
17. D. W. Moore, in *Vortex Motion*, edited H. G. Hornung and E. A. Muller, p. 97 (1982).
18. G. R. Baker, D. I. Meiron, and S. A. Orszag, *Physica* **12D**, 19 (1984).
19. S. J. Karrila and S. Kim, *Chem. Eng. Commun.* **82**, 123 (1989).

20. N. A. Pelekasis, J. A. Tsamopoulos, and G. D. Manolis, *Phys. Fluids A* **2**, 1328 (1990).
21. N. A. Pelekasis, J. A. Tsamopoulos, and G. D. Manolis, *J. Fluid Mech.* **230**, 541 (1991).
22. P. L. Marston and R. E. Apfel, *J. Colloid Interface Sci.* **68**, 280 (1979).
23. M. C. Lee, I. A. Feng, D. D. Elleman, T. G. Wang, and A. T. Young, in *Proceedings Second International Colloquium on Drops and Bubbles*, edited D. H. Le Croissette (Jet Propulsion Laboratory, Pasadena, CA, 1982), p. 107.
24. E. Trinh, A. Zwern, and T. G. Wang, *J. Fluid Mech.* **115**, 453 (1982).
25. J. R. Carruthers and L. R. Testardi, *Ann. Rev. Mater. Sci.* **13**, 247 (1983).
26. J. W. S. Rayleigh, *Proc. R. Soc. London* **29**, 71 (1879).
27. J. A. Tsamopoulos and R. A. Brown, *Phys. Fluids* **30**, 27 (1987).
28. J. A. Tsamopoulos and R. A. Brown, *J. Fluid Mech.* **127**, 519 (1983).
29. C. T. Alonso, in *Proceedings International Colloquium on Drops and Bubbles*, edited by D. J. Collins, M. S. Plesset, and M. M. Saffren (Jet Propulsion Laboratory, Pasadena, CA, 1974).
30. G. B. Foote, *J. Comput. Phys.* **11**, 507 (1973).
31. R. E. Benner, *Equilibria Stability and Bifurcations in the Physics of Fluid Interfaces*, Ph.D. Thesis, University of Minnesota, 1983.
32. T. S. Lundgren and N. N. Mansour, *J. Fluid Mech.* **194**, 479 (1988).
33. V. E. Zakharov, *J. Appl. Mech. Phys.* **2**, 190 (1968) [transl. of *Zh. Prikl. Mekh. Tekh. Fiz.* **9** (2), 86].
34. J. W. Miles, *J. Fluid Mech.* **83**, 153 (1977).
35. G. R. Baker and M. J. Shelley, *J. Comput. Phys.* **64**, 112 (1986).
36. G. K. Batchelor, *Introduction to Fluid Dynamics* (Cambridge Univ. Press, Cambridge, 1967).
37. A. H. Stroud and D. Secrest, *Gaussian Quadrature Formulas* (Prentice–Hall, Englewood Cliffs, NJ, 1966).
38. G. Strang and G. Fix, *An Analysis of the Finite Element Methods* (Prentice–Hall, Englewood Cliffs, NJ, 1973).
39. C. de Boor, *A Practical Guide to Splines* (Springer-Verlag, New York, 1978).
40. M. Abramowitz and I. A. Stegun, *Handbook of Mathematical Functions* (Dover, New York, 1972).
41. J. C. Lachat and J. O. Watson, *Int. J. Numer. Methods Eng.* **10**, 991 (1976).
42. J. A. Tsamopoulos and R. A. Brown, *J. Fluid Mech.* **147**, 373 (1984).
43. N. A. Pelekasis, J. A. Tsamopoulos, and G. D. Manolis, in *Advances in Boundary Elements*, Vol. 2, edited by C. A. Brebbia and J. J. Connor (Springer, New York, 1989), p. 419.
44. J. D. Lambert, *Computational Methods in Ordinary Differential Equations* (Wiley, New York, 1973).
45. N. A. Pelekasis, *A Study on Drop and Bubble Dynamics via a Hybrid Boundary Element–Finite Element Methodology*, Ph.D. Thesis in Chemical Engineering, SUNY at Buffalo, Buffalo, New York, 1991.
46. N. A. Pelekasis and J. A. Tsamopoulos, submitted for publication.